

## School of Computer Science and Communication

A non-conforming finite element method for interface Stokes problems and its application to two-phase Rayleigh-Taylor instability with solid obstacles

Alexei Loubenets, Michael Hanke

TRITA-NA 2007:4

Alexei Loubenets, Michael Hanke
A non-conforming finite element method
for interface Stokes problems and its application
to two-phase Rayleigh-Taylor instability with solid obstacles

Report number: TRITA-NA 2007:4

ISSN 0348-2952

ISRN KTH/NA--07/04--SE

Publication date: September 2007 E-mail of author: alexei@nada.kth.se

#### Reports can be ordered from:

School of Computer Science and Communication (CSC) Numerical Analysis Royal Institute of Technology (KTH) SE-100 44 Stockholm SWEDEN

 $\begin{array}{l} telefax:\ +46\ 8\ 790\ 09\ 30 \\ http://www.csc.kth.se/ \end{array}$ 

# A non-conforming finite element method for interface Stokes problems and its application to two-phase Rayleigh-Taylor instability with solid obstacles

Alexei Loubenets, Michael Hanke September 14, 2007

#### Abstract

In this paper, we establish an immersed finite element method for the solution of interface Stokes problems. The main idea of the method is to use a fixed, uniform mesh everywhere over the computational domain except the vicinity of the interface, where specifically designed macro elements are employed, such that the jump conditions are well approximated. In general, the resulting immersed finite element space is non-conforming. The interface itself is represented with the help of Lagrangian markers. The capability of the method is illustrated in the case of a Rayleigh-Taylor two-phase flow instability problem with solid suspensions governed by the Stokes equations.

## 1 Introduction

The flow situation considered in this article is a variation of the classical viscous Rayleigh-Taylor (RT) flow problem that is often used in the literature to evaluate the performance of different interface tracking numerical methods. Physically, the RT problem is a fingering instability of an interface between two or more stratified fluids of different density subjected to acceleration, or in a vertical gravitational field. The interface becomes unstable for certain perturbations and these perturbations evolve into spikes of heavy fluid and bubbles of light fluid which penetrate into both fluids. This type of instability occurs in diverse applications, including mantle and lithosphere dynamics, diapirism, post-glacial rebound and many others. The experimental and analytical investigations of this instability were performed by, among others, Lewis [12], Chang and Watson [7], Daff, Harlow and Hirt [6], Popil and Curzon [18], Gertsenstein and Cherniavskii [9], Danilov and Omelyanov [4],[5], and Barnes [1]. It has been shown that the evolution of a RT instability is a complex phenomena that involves formation and detachment of droplets, development of Helmholtz

1 INTRODUCTION

instability on the side of the penetrating spikes, competition and amalgamation among the rising bubbles and etc.

Since then, many numerical methods have also been developed and applied to study this phenomena. Fraigneau et al. [8] developed an Eulerian method for simulating variable density incompressible viscous flows. They compared the finite element method and finite volume method for the RT problem in the viscous regime for two different Reynolds numbers. It was shown that, even at moderate Reynolds numbers, this problem is very sensitive to the numerical method used and, in particular, to the mesh refinement algorithm.

Rudman [22] used an algorithm for volume tracking based on the concept of flux-corrected transport (FCT) to solve the RT flow problem. He also compared his method with three other techniques: the simple line interface calculation (SLIC) method, the VOF method of Hirt and Nichols [11] and Young's method [30].

Zhao et al. [31] solved the incompressible Navier-Stokes equations for two superimposed viscous fluids on unstructured grids with the finite volume method. The free surface was computed with the VOF method and the surface tension was taken into account. The motion of the characteristic RT mushroom shape of the interface was studied at Re = 283. See [23] and [21] for the further references on VOF methods applied to RT instability.

Popinet and Zaleski in [19] revisited the work of Puckett *et al.* [20] and solved the RT flow problem with the front-tracking technique. A source term was added to account for the surface tension forces as well. Glimm *et al.* have successfully applied front-tracking method to three dimension, as well as extending the front tracking capabilities to deal with the topological changes in the interface [10]. Similar work has been done by Tryggvason and Unverdi in [27], [29] and [28].

The level set method has also been extensively used in the simulation of the RT flow problems, see [25] and [32] for further references.

In this paper, we will employ an alternative approach that is also an Eulerian model, the immersed interface finite element method. This approach, originally proposed by Li in [13], [14] and extended in [15], [16], [17] uses a triangulation that is independent of the interface. The interface itself is represented by an additional structure (t.ex. markers with a parametric description) that is continuously updated using some information obtained from uniform background mesh.

The main idea of the method is to separate the elements of the background mesh into two classes, the ones that are intersected by the interface and the rest. On the non-intersected elements we use standard linear polynomials. On the intersected elements we use a strategy similar to that of the Hsieh-Clough-Tocher macro-element [2]. That is, each intersected element is subdivided by the interface into two subdomains. Then, we construct a  $C^0$  function consisting of piecewise linear polynomials on each of the subdomains such that the element has a total of 4 degrees of freedom. At the vertices of the original element, we specify the function values. The additional degrees of freedom are satisfied by the approximation of the jump conditions. Since this procedure involves subpartition of the original triangle, we can regard the intersected elements as macro-elements. The resulting immersed finite element space over the entire domain is, in general, non-conforming.

The objective of this paper is twofold. First we aim at extending the capabilities of the

immersed interface finite element method that was recently developed and analyzed for the elliptic interface problems ([13],[14],[15], [16] and [17]). This extension should allow our method to handle the Stokes interface problems. In addition, solid obstacles are included in the computational domain. That should be regarded as a first step in a practical direction of having suspensions in the flow. Note, that in reference [15] the interface Stokes problem is solved by decoupling the equations into three separate Poisson problems, one for pressure and two for the velocity components. That was possible due to the periodic boundary conditions that were used and homogeneity of the physical fields. In the present work, the Stokes equations are not decoupled, the physical fields are discontinuous and singular source terms are present. The method will be used to solve the Rayleigh-Taylor instability problem. The investigation will mainly concern the effect of the density gradient, shape of the computational domain and the amount and structure of the solid obstacles on the dynamics of the interface.

The rest of the paper is organized in the following way. The problem formulation and its background are given in Section 2. The method description is presented in Section 3. This is followed numerical examples and conclusions.

## 2 Problem formulation

In this chapter we introduce the Rayleigh-Taylor two-phase flow instability problem with solid obstacles governed by the Stokes equations. We describe the typical dynamics of the interface in the classical Rayleigh-Taylor instability, introduce the variational formulation of the problem and, finally, derive the jump conditions across the interface.

## 2.1 Rayleigh-Taylor instability problem

Let us consider the flow of two immiscible and incompressible fluids in the following two-dimensional domain

$$\Omega = \{ x \in \mathbb{R}^2 | \quad 0 < x < 2L, \quad -L < y < L \} \setminus \bigcup_i \overline{\Omega}_i,$$

where each rectangular subdomain  $\Omega_i$  represents a single solid obstacle

$$\Omega_i = \{ x \in \mathbb{R}^2 | \quad a_i < x < b_i, \quad c_i < y < d_i \}$$

for some  $a_i, b_i, c_i, d_i \in \mathbb{R}$ , see Figure 1. Let, initially, the interface between two immiscible liquids be

$$\Gamma = \{x \in \mathbb{R}^2 | y = h(x), x \in [s_1, s_2] \subseteq [0, 2L]\},\$$

where h is some  $C^{\infty}$ , L-periodic function. Then the interface  $\Gamma$  divides the domain  $\Omega$  into

$$\Omega^{+} = \{-L < y < h(x), \quad 0 < x < 2L\} \setminus \cup \overline{\Omega}_{i},$$
  
$$\Omega^{-} = \{h(x) < y < L, \quad 0 < x < 2L\} \setminus \cup \overline{\Omega}_{i}.$$

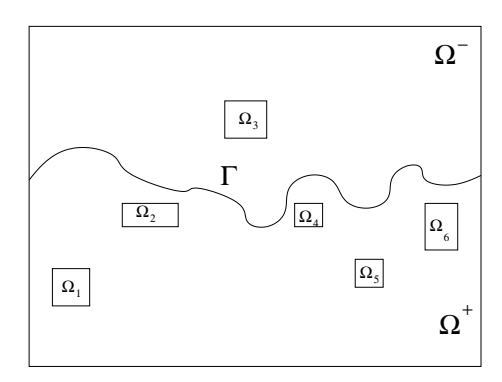


Figure 1: The computational domain  $\Omega$  and its partition by the interface  $\Gamma$ .

Let

$$\mathbf{u}:\Omega\to\mathbf{R}^2,\quad p:\Omega\to\mathbf{R}$$

be the velocity vector and the pressure. Denote by  $\rho$  and  $\mu$  the piecewise constant kinematic density and viscosity of the two fluids

$$\rho = \begin{cases}
\rho^{+} & \text{for } x \in \Omega^{+}, \\
\rho^{-} & \text{for } x \in \Omega^{-},
\end{cases}, \quad \mu = \begin{cases}
\mu^{+} & \text{for } x \in \Omega^{+}, \\
\mu^{-} & \text{for } x \in \Omega^{-}.
\end{cases}$$
(1)

Moreover, denote by  $\mathbf{X}(s,t) = (X(s,t),Y(s,t))$  the location of the interface  $\Gamma$  at some moment time t parameterized with respect to the arclength s. Then the dynamics of two immiscible and incompressible fluids in computational domain  $\Omega$  is described by the Stokes equations

$$\mu \Delta \mathbf{u} - \nabla p = \rho \mathbf{g} + \mathbf{f} \delta_{\Gamma}, \quad x \in \Omega,$$

$$\nabla \cdot \mathbf{u} = 0, \quad x \in \Omega \backslash \Gamma,$$
(2)

together with the Cauchy problem for the interface

$$\frac{\partial}{\partial t} \mathbf{X}(s,t) = \mathbf{u}(\mathbf{X}(s,t),t),$$
$$\mathbf{X}(s,0) = (s,h(s)).$$

Here,  $\mathbf{g} = (0, 1)$  is the gravitational constant and the source term  $\mathbf{f}\delta_{\Gamma}$  describes either tension or an elastic force acting along the interface with force density  $\mathbf{f} = (f_1, f_2)$ . We pose no-slip boundary conditions on the upper and lower bases of the domain  $\Omega$  and the periodicity condition on its lateral sides

$$\mathbf{u}\Big|_{y=\pm L} = 0, \quad \frac{\partial^k \mathbf{u}}{\partial x^k}\Big|_{x=0} = \frac{\partial^k \mathbf{u}}{\partial x^k}\Big|_{x=2L}, \qquad k = 0, 1.$$

No-slip boundary conditions are also imposed on the boundaries of the solid suspensions

$$\mathbf{u}|_{\cup\partial\Omega_i}=0.$$

The interface  $\Gamma$  between the liquids has the same velocity as the surrounding fluids.

The behavior of the classical RT instability problem (without solid obstacles) is usually divided into four separate stages [24]. The first stage is dominated by the small growth of the perturbations. As analyzed by the linear stability theory, the growth rate depends on the fluid's density gradient, viscosities, surface tension and compressibility (if applicable). The linear theory is no longer applicable after the perturbation grows to more than 10–40% of its original size. The second stage is characterized by the nonlinear perturbation growth, formation of the bubbles of light fluid threading through heavy fluid and emergence of the spikes of the heavy fluid that falls into the light fluid. During this stage, the nonlinear growth of perturbations is strongly influenced by the density ratio and three-dimensional effects. Interactions and amalgamations among the bubbles and the mushroom-shaped spikes are characteristics of this stage. Finally, this interaction evolves into a turbulent or chaotic mixing which dominates the fourth stage of the instability. In this final stage, phenomena such as the penetration of a bubble through a slab of fluid of finite thickness, necking, breakup of the spikes by various mechanism, and other complicated, topology related effects take place.

#### 2.2 Variational formulation and jump conditions

Consider problem (2) in the distributional sense. That is we view all the terms in the equations as distributions acting on any smooth functions  $\phi$  and  $\psi$ . Integrating by parts in (2) and summing up the momentum equations we obtain the following saddle point problem: Find  $(u, p) \in H_0^1(\Omega)^2 \times L_0^2(\Omega)$  such that

$$-\sum_{m=1}^{2} \iint_{\Omega} \mu \nabla u_{m} \cdot \nabla \psi_{m} dx + \iint_{\Omega} p \nabla \cdot \psi dx =$$

$$\sum_{m=1}^{2} \iint_{\Omega} \rho g_{m} \psi_{m} dx + \sum_{m=1}^{2} \int_{\Gamma} f_{m} \psi_{m} ds, \quad \forall \psi = (\psi_{1}, \psi_{2}) \in H_{0}^{1}(\Omega)^{2},$$

$$\iint_{\Omega} \phi \nabla \cdot u dx = 0, \quad \forall \phi \in L^{2}(\Omega),$$

$$(3)$$

where  $\rho$ ,  $\mu$  are given by (1).

**Theorem 2.1.** The first velocity component  $u_1$  satisfies the following jump conditions at the interface  $\Gamma$ 

$$[u_1]|_{\Gamma} = F_1, \quad \left[\mu \frac{\partial u_1}{\partial n}\right]|_{\Gamma} = F_2,$$
 (4)

where  $F_1 = 0$  and  $F_2 = [p] \cos(\Theta) - f_1$ . Here n is the outward unit normal vector to  $\Omega^-$  and  $\theta$  is an angle between a normal vector n and x-axis.

*Proof.* Consider the equivalent classical formulation of the first momentum eq. (2). Namely

$$\mu \Delta u_1 - \frac{\partial p}{\partial x} = \rho g_1, \quad (x, y) \in \Omega \backslash \Gamma.$$

Multiply by a sufficiently smooth test function  $\psi \in \mathcal{D}(\Omega)$  and integrate we obtain:

$$\iint_{\Omega^{\pm}} \mu \Delta u_1 \psi dx - \iint_{\Omega^{\pm}} \frac{\partial p}{\partial x} \psi dx = \iint_{\Omega^{\pm}} \rho^{\pm} g_1 \psi dx, \tag{5}$$

where, - and + signs indicates whether we approach interface  $\Gamma$  from  $\Omega^-$  or  $\Omega^+$ , correspondingly. Apply Greens theorem to the first term of the left hand side for each of the domains

$$\iint_{\Omega^{+}} \mu \Delta u_{1} \psi dx = -\int_{\Gamma} \mu (\nabla u_{1}^{+} \cdot n) \psi ds - \iint_{\Omega^{+}} \mu (\nabla u_{1} \cdot \nabla \psi) dx, 
\iint_{\Omega^{-}} \mu \Delta u_{1} \psi dx = \int_{\Gamma} \mu (\nabla u_{1}^{-} \cdot n) \phi ds - \iint_{\Omega^{-}} \mu (\nabla u_{1} \cdot \nabla \psi) dx. \tag{6}$$

Similarly, we rewrite the integral over pressure in (5) as

$$\iint_{\Omega^{+}} \frac{\partial p}{\partial x} \psi dx = -\int_{\Gamma} \psi([p^{+}, 0]^{T} \cdot n) ds + \iint_{\Omega^{+}} \left[ \frac{\partial \psi}{\partial x}, \frac{\partial \psi}{\partial y} \right]^{T} \cdot [p, 0]^{T} dx, 
\iint_{\Omega^{-}} \frac{\partial p}{\partial x} \psi dx = \int_{\Gamma} \psi([p^{-}, 0]^{T} \cdot n) ds + \iint_{\Omega^{-}} \left[ \frac{\partial \psi}{\partial x}, \frac{\partial \psi}{\partial y} \right]^{T} \cdot [p, 0]^{T} dx.$$
(7)

Insert (7) and (6) in (5) to obtain the following formulation

$$\iint_{\Omega} (-\mu \nabla u_1 \cdot \nabla \psi + p \frac{\partial \psi}{\partial x}) dx + \int_{\Gamma} [p] \cos(\theta) \psi ds - \int_{\Gamma} [\mu \frac{\partial u_1}{\partial n}] \psi ds = \iint_{\Omega} \rho g_1 \psi dx. \quad (8)$$

Consider now the first momentum eq. (2) in the distributional sense on the whole of  $\Omega$ . Multiplying by a sufficiently smooth test function  $\psi \in \mathcal{D}(\Omega)$  and integrating by parts we obtain

$$\iint_{\Omega} -\mu \nabla u_1 \cdot \nabla \psi dx + \iint_{\Omega} p \frac{\partial \phi}{\partial x} dx = \int_{\Gamma} f_1 \phi ds + \iint_{\Omega} \rho g_1 \psi dx, \quad \forall \psi \in \mathcal{D}(\Omega). \tag{9}$$

Since the test function is arbitrary, equations (9) and (8) are equal and thus

$$[u_1]|_{\Gamma} = 0$$
 and  $\left[\mu \frac{\partial u_1}{\partial n}\right]|_{\Gamma} = [p]\cos(\Theta) - f_1.$ 

**Theorem 2.2.** The second velocity component  $u_2$  satisfies the following jump conditions at the interface  $\Gamma$ 

$$[u_2]|_{\Gamma} = F_3, \quad \left[\mu \frac{\partial u_2}{\partial n}\right]|_{\Gamma} = F_4,$$
 (10)

where  $F_3 = 0$  and  $F_4 = [p]\sin(\Theta) - f_2$ .

*Proof.* The proof is similar to that of the Theorem 2.1.

**Theorem 2.3.** The pressure p is subject to the following jump conditions at the interface  $\Gamma$ 

$$[p]|_{\Gamma} = F_5, \quad \left[\frac{\partial p}{\partial n}\right]|_{\Gamma} = F_6,$$
 (11)

where  $F_5 = \hat{f}_1$  and  $F_6 = \frac{\partial \hat{f}_2}{\partial \tau}$ . Here  $\tau$  is the tangent unit normal vector to  $\Gamma$  and  $\hat{f}_1, \hat{f}_2$  are the normal and tangential components of the force density  $f = (f_1, f_2)$ , correspondingly.

*Proof.* To simplify the proof, we reduce (2) to the pressure Poisson problem. That is we multiply the momentum equations with some smooth test function  $\phi \in \mathcal{D}(\Omega)$ , differentiate (in the distributional sense) the first equation with respect to x, the second with respect to y, add the resulting equations together and use the continuity equation to obtain

$$\langle \Delta p, \phi \rangle = \langle \nabla \cdot (f \delta_{\Gamma}), \phi \rangle, \quad \forall \phi \in \mathcal{D}(\Omega),$$
 (12)

where  $\langle \cdot, \phi \rangle$  denotes the action of the distribution on the test function  $\phi$ . Recalling the definition of the distribution and its derivative, we end up with

$$\iint_{\Omega} p\Delta\phi dx = -\int_{\Gamma} f_1 \frac{\partial \phi}{\partial x} ds - \int_{\Gamma} f_2 \frac{\partial \phi}{\partial y} ds, \quad \forall \psi \in \mathcal{D}(\Omega).$$

For the sake of simplicity, we express  $\frac{\partial \phi}{\partial x}$  and  $\frac{\partial \phi}{\partial y}$  in terms of the normal and tangential derivatives along the interface  $\Gamma$ 

$$\frac{\partial \phi}{\partial x} = \frac{\partial \phi}{\partial n} \cos(\Theta) - \frac{\partial \phi}{\partial \tau} \sin(\Theta),$$
$$\frac{\partial \phi}{\partial y} = \frac{\partial \phi}{\partial n} \sin(\Theta) + \frac{\partial \phi}{\partial \tau} \cos(\Theta).$$

Then

$$\int_{\Gamma} (f_1 \frac{\partial \phi}{\partial x} + f_2 \frac{\partial \phi}{\partial y}) ds = \int_{\Gamma} \left( (f_1 \cos(\Theta) + f_2 \sin(\Theta)) \frac{\partial \phi}{\partial n} + (f_2 \cos(\Theta) - f_1 \sin(\Theta)) \frac{\partial \phi}{\partial \tau} \right) ds = \int_{\Gamma} (\hat{f}_1 \frac{\partial \phi}{\partial n} + \hat{f}_2 \frac{\partial \phi}{\partial \tau}) ds,$$

where  $\hat{f}_1$  and  $\hat{f}_2$  are correspondingly the normal and tangential components of the force density f

$$\hat{f}_1 = f_1 \cos(\Theta) + f_2 \sin(\Theta),$$
  
$$\hat{f}_2 = -f_1 \sin(\Theta) + f_2 \cos(\Theta).$$

Integrating the second term by parts and using the periodicity in  $\Gamma$  we obtain

$$\int_{\Gamma} \hat{f}_2 \frac{\partial}{\partial \tau} \phi ds = \hat{f}_2 \phi|_{s=s_2} - \hat{f}_2 \phi|_{s=s_1} - \int_{\Gamma} \frac{\partial \hat{f}_2}{\partial \tau} \phi ds = - \int_{\Gamma} \frac{\partial \hat{f}_2}{\partial \tau} \phi ds.$$

Then

$$\iint_{\Omega} p\Delta\phi dx = \int_{\Gamma} \frac{\partial \hat{f}_2}{\partial \tau} \phi - \hat{f}_1 \frac{\partial \phi}{\partial n} ds. \tag{13}$$

Consider now the eq. (12) separately on  $\Omega^+$  and  $\Omega^-$  and apply Greens formula twice to the left hand side we get

$$\iint_{\Omega^{+}} \Delta p \phi dx = \iint_{\Omega^{+}} p \Delta \phi dx - \int_{\Gamma} \frac{\partial p^{+}}{\partial n} \phi ds + \int_{\Gamma} p^{+} \frac{\partial \phi}{\partial n} ds, 
\iint_{\Omega^{-}} \Delta p \phi dx = \iint_{\Omega^{-}} p \Delta \phi dx + \int_{\Gamma} \frac{\partial p^{-}}{\partial n} \phi ds - \int_{\Gamma} p^{-} \frac{\partial \phi}{\partial n} ds.$$
(14)

Add equations (14) together to obtain

$$\iint_{\Omega} p\Delta\phi dx - \int_{\Gamma} \left[\frac{\partial p}{\partial n}\right] \phi ds + \int_{\Gamma} [p] \frac{\partial \phi}{\partial n} ds = 0, \quad \forall \phi \in \mathcal{D}(\Omega).$$

Compare this equation with (13) and use the fact that  $\phi$  is arbitrary we get the following jump conditions

$$[p]|_{\Gamma} = \hat{f}_1$$
 and  $\left[\frac{\partial p}{\partial n}\right]_{\Gamma} = (\nabla \hat{f}_2 \cdot \tau).$ 

**Remark 1.** Note that with the help of Theorem 2.3 we can rewrite the flux jump condition for the velocity vector as

$$\left[\mu \frac{\partial u_1}{\partial n}\right]\Big|_{\Gamma} = [p]\cos(\Theta) - f_1 = \hat{f}_2\sin\Theta, \qquad \left[\mu \frac{\partial u_2}{\partial n}\right]\Big|_{\Gamma} = [p]\sin(\Theta) - f_2 = -\hat{f}_2\cos\Theta.$$

## 3 Finite element formulation

In this section, we discuss the approximation of the interface, construction of the specific macro-elements that will approximate the jump conditions, introduce our non-conforming immersed interface finite element spaces and, finally, present the finite element formulation of our problem.

The Taylor-Hood element [2] is an often-used triangular element where the velocity polynomial has a higher degree than the pressure polynomial and thus the LBB stability condition (inf-sup) is satisfied. In this paper, we will employ the modified Taylor-Hood element. That is, with h as the discretization step, we introduce triangulation  $\mathcal{T}_{2h} = \{T\}$  of the domain  $\Omega$  for the pressure. This triangulation is not aligned with the interface  $\Gamma$  and satisfies the following standard conditions:

- $\bar{\Omega} = \bigcup_{T \in \mathcal{T}_{2h}} T$ ,
- If  $T_1, T_2 \in \mathcal{T}_{2h}$  and  $T_1 \neq T_2$ , then either  $T_1 \cap T_2 = \emptyset$  or  $T_1 \cap T_2$  is a common vertex or edge of both triangles,

• The triangulation is assumed to be uniform i.e. there are two positive constants independent of h such that

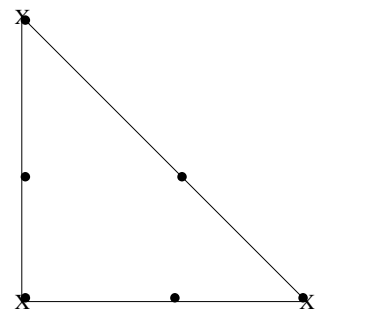
$$C_0 \rho_T \leq h \leq C_1 \bar{\rho}_T$$

where, for all  $T \in \mathcal{T}_h$ ,  $\rho_T$  and  $\bar{\rho}_T$  stands for the diameters of inscribed and circumscribed circles, respectively,

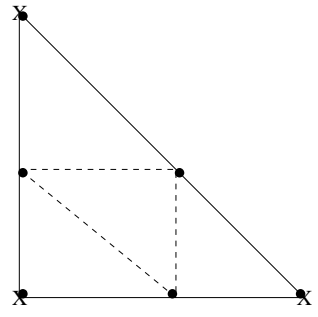
together with the following compatibility conditions with the interface  $\Gamma$ 

- If  $\Gamma$  meets a triangle T at two points, then these points must be on different edges of this triangle,
- If  $\Gamma$  meets one edge of a triangle at more than two points, then this edge is a part of  $\Gamma$ .

For the velocity field, we introduce an additional, twice finer triangulation  $\mathcal{T}_h$  that satisfies the same standard and compatibility conditions as  $\mathcal{T}_{2h}$ . That is achieved by subdiving each pressure element into four congruent velocity subtriangles, see Figure 2. Thus, the number of degrees of freedom is the same as for the standard Taylor-Hood element.



(a) The classical  $\mathcal{P}2$ -iso- $\mathcal{P}1$  Taylor-Hood element. Same mesh is used for both velocity and pressure.



(b) The modified  $\mathcal{P}1$ -iso- $\mathcal{P}1$  Taylor-Hood element. Twice finer mesh is used for the velocity field.

Figure 2: The Taylor-Hood elements. Here the velocity field u is given at the nodes ( $\bullet$ ) and the pressure p at the nodes ( $\times$ ).

We are now ready to consider the construction of the finite element functions on an interface elements. The main idea is to separate the elements of the partition in two classes, the one that are intersected by the interface and the rest. On the non-intersected elements we use the standard linear polynomials for pressure and velocity fields. On the intersected elements we use a strategy similar to that of the Hsieh-Clough-Tocher macro-element [2]. That is, each intersected element is subdivided by the interface in two subdomains. Then, we construct a  $C^0$  function consisting of piecewise linear polynomials such that the element has a total of 6 degrees of freedom. At the vertices of the original element, we specify the function values. The additional degrees of freedom are satisfied by the approximation of

the jump conditions. Since this procedure involves subpartition of the original triangle, we can regard the intersected elements as macro-elements.

Denote by  $\mathcal{T}'_h$  the set of all elements in the triangulation  $\mathcal{T}_h$  that are intersected by the interface  $\Gamma$  (interface elements). By the construction, the interface  $\Gamma$  can meet the element  $T \in \mathcal{T}'_h$  at most at two edges. Denote these intersection points by  $A = (x_A, y_A)$  and  $B = (x_B, y_B)$  and use  $\mathbf{Z}_1 = (x_1, y_1)$ ,  $\mathbf{Z}_2 = (x_2, y_2)$  and  $\mathbf{Z}_3 = (x_3, y_3)$  to denote the vertices of the triangle. Let  $m_h$  denote the total number of the intersected triangles. Then, we represent the interface  $\Gamma$  and its piecewise linear approximation  $\Gamma_h$  as

$$\Gamma = \bigcup_{r=1}^{m_h} \Gamma^r$$
 and  $\Gamma_h = \bigcup_{r=1}^{m_h} \Gamma_h^r$ ,

where the arc segment  $\Gamma^r = \Gamma \cap T^r$  for some  $T^r \in \mathcal{T}'_h$  and  $\Gamma^r_h = \overline{AB}$  is the linear approximation of  $\Gamma^r$ , see Fig. 3.

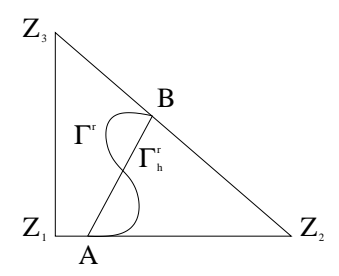


Figure 3: The arc segment  $\Gamma^r$  and its linear approximation  $\Gamma^r_h$ .

In addition, each  $T \in \mathcal{T}'_h$  is subdivided by the corresponding linear segment  $\Gamma^r_h$  into two subdomains  $T^-$  and  $T^+$ , see Figure 4. Similarly, we construct the elements of the  $\mathcal{T}'_{2h}$  triangulation. Note, that both triangulations share the same interface representation  $\Gamma_h$ . At this point, we should also mention that this particular representation of the interface introduces a  $O(h^2)$  error in the solution [3].

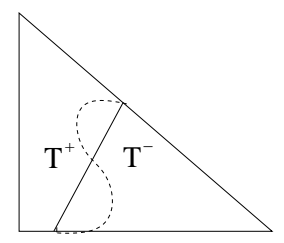


Figure 4: Subdomains  $T^+$  and  $T^-$  are formed by  $\Gamma^r_h$ .

The idea now is to use the partition of  $T \in \mathcal{T}'_h$  generated by the approximation of the interface  $\Gamma_h$  in order to approximate the jump conditions. That is, for each interface triangle we form a finite element function by two polynomials defined separately on  $T^-$ 

and  $T^+$ 

$$\psi_h(x,y) = \begin{cases} \psi_h^-(x,y) = a_1 x + a_2 y + a_3, & x \in T^-, \\ \psi_h^+(x,y) = b_1 x + b_2 y + b_3, & x \in T^+. \end{cases}$$
(15)

Then for all  $T \in \mathcal{T}'_h$  define a linear space

$$S_h(T) = \begin{cases} \psi_h \text{ is defined by (15),} \\ \psi_h^-(A) = \psi_h^+(A), & \psi_h^-(B) = \psi_h^+(B), \end{cases}$$

that consists of the piecewise linear functions satisfying the continuity conditions along  $\Gamma_h$ . Define

$$Q_{\Gamma_h^r}(\psi_h) := \int_{\Gamma_h^r} (\mu_h^- \nabla \psi_h^- - \mu_h^+ \nabla \psi_h^+) \cdot \mathbf{n}_{\Gamma_h^r} ds,$$

where  $\mathbf{n}_{\Gamma_h^r}$  is the unit normal vector to line segment  $\Gamma_h^r$  and  $\mu_h$  stands for the approximation of the coefficient function  $\mu(x,y)$  that is equal to  $\mu$  on the non-interface elements and is defined as follows

$$\mu_h(x,y) = \begin{cases} \mu^-, & \forall (x,y) \in T^-, \\ \mu^+, & \forall (x,y) \in T^+ \end{cases}$$

$$\tag{16}$$

for any  $T \in \mathcal{T}'_h$ . Note, that  $\mu_h$  is just a restriction/prolongation of the piecewise constant function  $\mu$ . We now introduce the following affine space that consists of the piecewise linear functions that satisfy standard interpolation conditions on the function itself together with the specific interpolation condition on the line integral over a jump in the flux of the function

$$S_h^0(T) = \{ \psi_h \in S_h(T) |, \quad \psi_h(\mathbf{Z}_i) = u_m(\mathbf{Z}_i), \quad Q_{\Gamma_h^r}(\psi_h) = 0 \}.$$

We use the partition  $\mathcal{T}_h$  to define immersed finite element spaces on the whole of  $\Omega$ . Namely,

$$V_h(\Omega) = \Big\{ \psi_h \in C(\overline{\Omega})^2 \cap H_0^1(\Omega)^2; \quad \psi_h|_T \in S_h(T), \forall T \in \mathcal{T}_h \Big\},$$
$$V_h^0(\Omega) = \Big\{ \psi_h \in V_h(\Omega); \quad \psi_h|_T \in S_h^0(T), \forall T \in \mathcal{T}_h' \Big\}.$$

In addition, we denote by  $V_{h,0}^0$  the subspace of  $V_h^0$  with its functions vanishing on the Dirichlet part of the boundary  $\partial\Omega$ . In a similar fashion, we define the pressure spaces. Namely, let  $\forall T \in \mathcal{T}'_{2h}$ 

$$M_h(T) = \begin{cases} \phi_h \text{ is defined by (15),} \\ \phi_h^-(A) = \phi_h^+(A), & \phi_h^-(B) = \phi_h^+(B), \end{cases}$$

and

$$W_{\Gamma_h^r}(\phi_h) := \int_{\Gamma_h^r} (\nabla \phi_h^- - \nabla \phi_h^+) \cdot \mathbf{n}_{\Gamma_h^r} ds.$$

Then

$$M_h^0(T) = \{ \phi_h \in M_h(T) |, \quad \phi_h(\mathbf{Z}_i) = p(\mathbf{Z}_i), \quad W_{\Gamma_h^r}(\phi_h) = 0 \}.$$

In order to accommodate the jump in pressure, we introduce an additional affine space

$$\tilde{M}_h(T) = \begin{cases} \phi_h \text{ is defined by (15),} \\ \phi_h^-(A) - \phi_h^+(A) = F_5(A), & \phi_h^-(B) - \phi_h^+(B) = F_5(B), \end{cases}$$

where  $F_5$  is given in Theorem 2.3. Note, that the elements of  $\tilde{M}_h(T)$  are the  $L^2$  functions approximating the pressure jump condition at the intersection points A, B. As in the case of the velocity field, we use the partition  $\mathcal{T}_{2h}$  to define the global spaces  $M_h(\Omega)$ ,  $M_h^0(\Omega)$  and  $\tilde{M}_h(\Omega)$  as follows

$$M_h(\Omega) = \left\{ \phi_h \in C(\overline{\Omega}) \cap L_0^2(\Omega); \quad v_h|_T \in M_h(T), \forall T \in \mathcal{T}_{2h} \right\},$$

$$\tilde{M}_h(\Omega) = \left\{ \phi_h \in C(\overline{\Omega}) \cap L_0^2(\Omega); \quad \phi_h|_T \in \tilde{M}_h(T), \forall T \in \mathcal{T}'_{2h} \right\},$$

$$M_h^0(\Omega) = \left\{ \phi_h \in M_h(\Omega); \quad \phi_h|_T \in M_h^0(T), \forall T \in \mathcal{T}'_{2h} \right\}.$$

Then, the discrete solutions of (3) are represented by the linear combinations

$$u_{m,h} = \tilde{u}_{m,h} + u_{m,h}^N, \quad m = 1, 2 \quad \text{and} \qquad p_h = \tilde{p}_h + \sum_{i=1}^2 p_h^{N,i},$$

where

$$\tilde{u}_{m,h} = \sum_{j} U_{m,j} \psi_{m,j}, \qquad \tilde{p}_h = \sum_{k} P_k \phi_k,$$

with  $\psi_{m,j} \in V_{h,0}^0(\Omega)$  and  $\phi_k \in M_h^0(\Omega)$ . It holds

$$[\tilde{u}_{m,h}]_{\Gamma_h} = 0, \quad \left[\mu_h \frac{\partial \tilde{u}_{m,h}}{\partial n}\right]_{\Gamma_h} = 0,$$

$$[\tilde{p}_h]_{\Gamma_h} = 0, \quad \left[\frac{\partial \tilde{p}_h}{\partial n}\right]_{\Gamma_h} = 0.$$
(17)

Note, that the actual jump conditions (4), (10) and (11) have been approximated by the explicitly constructed functions  $u_{1,h}^N, u_{2,h}^N \in V_h(\Omega)$ , and  $p_h^{N,1} \in M_h(\Omega)$ ,  $p_h^{N,2} \in \tilde{M}_h(\Omega)$ , with the following interpolation conditions

$$u_{1,h}^{N}(\mathbf{Z}_{i}) = 0, \quad Q_{\Gamma_{h}^{r}}(u_{h}^{N,1}) = \int_{\Gamma_{h}^{r}} F_{2}ds,$$

$$u_{2,h}^{N}(\mathbf{Z}_{i}) = 0, \quad Q_{\Gamma_{h}^{r}}(u_{h}^{N,2}) = \int_{\Gamma_{h}^{r}} F_{4}ds,$$

$$p_{h}^{N,1}(\mathbf{Z}_{i}) = 0, \quad W_{\Gamma_{h}^{r}}(p_{h}^{N,1}) = \int_{\Gamma_{h}^{r}} F_{6}ds,$$

$$p_{h}^{N,2}(\mathbf{Z}_{i}) = 0, \quad W_{\Gamma_{h}^{r}}(p_{h}^{N,2}) = 0.$$

Then, the varitational formulation of the saddle point (3) reads: Find  $\mathbf{u}_h = (u_{1,h}, u_{2,h}) \in V_h^0$  and  $\tilde{p}_h \in M_h^0$ 

$$-\sum_{m=1}^{2} \iint_{\Omega} \mu_{h} \nabla \tilde{u}_{m,h} \cdot \nabla \psi_{m,h} dx + \iint_{\Omega} \tilde{p} \nabla \cdot \psi_{h} dx =$$

$$\sum_{m=1}^{2} \iint_{\Omega} \rho_{h} g_{m} \psi_{m,h} dx + \sum_{m=1}^{2} \int_{\Gamma} f_{m} \psi_{m,h} dx + \sum_{m=1}^{2} \iint_{\Omega} \mu_{h} \nabla u_{m,h}^{N} \cdot \nabla \psi_{m,h} dx$$

$$+ \iint_{\Omega} p_{h}^{N,i} \nabla \cdot \psi_{m,h} dx, \quad \forall \psi_{m} = (\psi_{1,h}, \psi_{2,h}) \in V_{h}^{0}, \quad m = 1, 2,$$

$$\iint_{\Omega} \phi_{h} \nabla \cdot \tilde{u}_{h} dx = -\iint_{\Omega} \phi_{h} \left( \frac{\partial u_{1,h}^{N}}{\partial x} + \frac{\partial u_{2,h}^{N}}{\partial y} \right) dx, \quad \forall \phi_{h} \in M_{h}^{0}, \quad (18)$$

where  $\mu_h$  is given in (16) and  $\rho_h$  is defined in the similar fashion.

#### 3.1 Interface propagation

For the approximation of the interface  $\Gamma$  the Lagrangian markers are used. That is at any moment in time  $t_n$ , the interface is described by a given finite set of control points  $\mathbf{X}_k^n = \{X_k^n, Y_k^n\}$  for  $k = 0, 1, ..., m_h$ , together with the piecewise linear reconstruction between these points. Here, kth control point gives an approximation to  $(X(s_k, t_n), Y(s_k, t_n))$  where s is an arclength parameterization of the interface. The surface forces are calculated at the control points first and then spread all along the interface using linear interpolation.

To advect the interface, a two-step Runge-Kutta scheme is employed,

$$\tilde{\mathbf{X}}_{k} = \mathbf{X}_{k}^{n} + \Delta t \mathbf{U}_{k}^{n}, 
\tilde{\mathbf{X}}_{k} = \tilde{\mathbf{X}}_{k} + \Delta t \tilde{\mathbf{U}}_{k}^{n}, 
\mathbf{X}_{k}^{n+1} = (\tilde{\mathbf{X}}_{k} + \tilde{\tilde{\mathbf{X}}}_{k})/2,$$
(19)

where the local velocities  $\mathbf{U}_k^n$  and  $\tilde{\mathbf{U}}_k^n$  are obtained by interpolating the velocity field  $\{u_1^n,u_2^n\}$  at the control points  $\mathbf{X}_k^n$  and  $\tilde{\mathbf{X}}_k$  correspondingly. This interpolation is complicated by the fact that the velocity field has jumps in the normal derivatives across the interface. Thus the usual bilinear interpolation scheme cannot be applied in this case. A modified interpolation scheme is required such that the jump conditions for velocity field (4) and (10) are accounted for. In the case of this paper, we will employ the finite element spaces  $V_h^0(\Omega)$  and  $V_h(\Omega)$  to do the job. Namely, to obtain local velocities  $\mathbf{U}_k^n = (U_k^n, V_k^n)$  at control point  $\{X_k^n, Y_k^n\}$  we choose the three closest grid points  $(x_1, y_1), (x_2, y_2)$  and  $(x_3, y_3)$  (which will typically be the nodes of the triangular element containing the control point  $\{X_k^n, Y_k^n\}$ ) and form a linear combination of these values to obtain, say  $U_k^n$ 

$$U_k^n = \psi_1(X_k^n, Y_k^n)u(x_1, y_1) + \psi_2(X_k^n, Y_k^n)u(x_2, y_2) + \psi_3(X_k^n, Y_k^n)u(x_3, y_3) + u_{1,h}^N(X_k^n, Y_k^n)$$
(20)

where  $u(x_i, y_i)$  is the grid velocity corresponding to the point  $(x_i, y_i)$ ,  $\psi_i(X_k^n, Y_k^n) \in V_h^0(\Omega)$  is the modified test function corresponding to node  $(x_i, y_i)$  and the explicitly constructed  $u_{1,h}^N \in V_h(\Omega)$  corresponding for the inhomogeneous jump in the normal flux of  $u_{1,h}^n$ . A similar procedure is used to obtain  $V_k^n$ .

To review, the numerical solution of the interface Stokes problem (2) is obtained by the following procedure:

- Use the location of the interface given by the set of the control points  $\{X_k^n, Y_k^n\}$  to compute the surface forces on the interface and jump conditions (4), (10) and (11).
- Obtain the background grid velocities  $\tilde{\mathbf{u}}_h = (u_{1,h}, u_{2,h})$  by solving the coupled Poisson problem (18) with the known jump conditions.
- Interpolate  $\tilde{\mathbf{u}}_h$  to compute the local velocities  $\mathbf{U}_k^n$  and  $\tilde{\mathbf{U}}_k^n$  at every control point using (20).
- Advect the interface with these velocities for time  $\Delta t$  using the two-step Runge-Kutta method (19).

The procedure is repeated for every time step  $\Delta t$ . This concludes our description of the immersed finite element method for the interface Stokes problem.

### 4 Numerical results

In this section we investigate the performance of immersed interface finite element methods applied to the RT instability problem. Two test cases are considered. In the first case we are interested in the fingering or "mushy" behavior of the interface. The solid obstacles are different in size and are randomly distributed in the computational domain. In the second test case, we consider a symmetric configuration with the solid obstacles of the same size. In both test cases, the initial configuration is unstable, in the sense that the heavy fluid is lying on top of the light one. The computational domain  $\Omega$  is a rectangle and the interface  $\Gamma$  is represented by some periodic curve.

The solution is approximated on a uniform  $n \times 2n$  Cartesian triangular mesh with  $m_h$  discrete points, representing the interface  $\Gamma$ . Since the exact solution is unknown we measure the accuracy of our method by using the extrapolation principle. That is, we investigate the error between two successive solutions  $e = u_n - u_{2n}$  for every resolution n. To measure the error we employ the discrete  $L^2$  norm defined by

$$||E_n||_{L^2} = h \sqrt{\sum_{i,j} e_{ij}^2}.$$

We also display the ratios between the successive errors

$$ratio = ||E_n||_{L^2}/||E_{2n}||_{L^2},$$

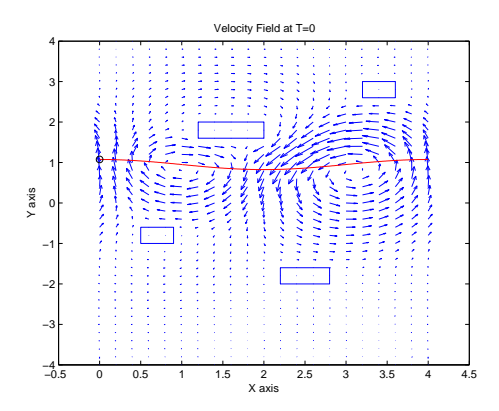


Figure 5: The initial configuration and the velocity field for test case 1 using  $80 \times 80$  uniform mesh.

where a ratio of 2 corresponds to first order accuracy, while a ratio of 4 indicates second order accuracy. At this point we should note, that any discretization error in the numerical solution will me magnified by the unstable nature of the flow (heavy fluid on-top the lighter one) and affect both the convergence study and other desirable properties of the flow, such as, for example, the symmetry (if applicable).

## 4.1 Test problem 1

The initial configuration is shown in Figure 5. As we can see, four solid rectangular particles are placed in both heavy and light fluids. The interface is represented by a cosine function. The other parameters were taken to be  $\mu^+ = \mu^- = 1$ ,  $\rho^- = 2$  and  $\rho^+ = 1$ . The force density was given by

$$\mathbf{f} = \sigma \kappa \mathbf{n}$$

where  $\sigma = 0.1$  is the surface tension coefficient,  $\kappa$  is is the curvature and  $\mathbf{n}$  is the normal vector to  $\Gamma$ . Note, that in all forthcoming pictures the plotting resolution is chosen to be coarser than the resolution of the obtained numerical solution.

First, we compute the solution at t=0, when the interface has not moved. As expected, the heavy fluid starts to fall down, while the light starts to rise. To measure the order of accuracy of our method a grid refinement study is performed. The solution  $(p, u_1 \text{ and } u_2)$  was computed on four different  $n \times 2n$  grids with n=40, 80, 160 and 320 and m=400 points on the interface.

As we can see from Table (4.1) the ratios are approaching 4 which is a clear indication of second order accuracy. We now consider the error at later times, when the interface has moved. The main difficulty in comparing the solution at all the points on the fixed grid comes from the fact that due to the unstable nature of the flow the interface may lie on one side of certain fixed grid point in one calculation, but slightly to the other side in a different calculation.

n	$p$ ratio in $L^2$ norm	$u_1$ ratio in $L^2$ norm	$u_2$ ratio in $L^2$ norm
40	3.1841	3.2131	3.1973
80	3.5322	3.7412	3.7092

Table 1: The ratio in the error between the successive solutions, i.e.  $e = p_n - p_{2n}$  and  $e = u_n - u_{2n}$  at t = 0 in  $L^2$  norm.

Since the area enclosed by the interface should be conserved we can use the mass conservation as a measure of the convergence of our method. Namely, for the fixed values of the time step  $\Delta t = 0.01$  and the background grid n = 80, we refine the resolution of the interface m and consider the error

$$E_m = A_0 - A_m$$

where  $A_0$  is the initial area of, say, the upper fluid and  $A_m$  is the area of upper fluid at some moment in time t = T with m points on the interface.

m	$ E_m $ at $t = 0.1$	ratio	$ E_m $ at $t = 1.0$	ratio
20	0.0322431	_	0.0189312	-
40	0.0086836	3.7131	0.0050331	3.8675
80	0.0022555	3.8498	0.0012407	3.9134
160	0.0005796	3.8912	0.0003061	3.9733

Table 2: Grid refinement study for the Stokes interface problem with  $\Delta t = 0.01$  on the  $80 \times 80$  mesh. The columns represent the error in the area at t = 0.1 and t = 1, correspondingly.

Table 2 shows the refinement study for T = 0.1 and T = 1. As we can see, the area is preserved with second-order accuracy using IIM FEM.

We now consider the qualitative behavior of the RT instability with time. Already at t=0 we can observe vortex formation due to the density gradient, see Figure 5. Driven by these vortices, the heavy fluid starts to fall down, while the light fluid is gradually rising, see Figures 6 - 9.

Already at t = 62.5 we can observe a beginning of what looks like threading or fingering of the heavy fluid, see Figure 10. At he same time the main bulk of the heavy fluid continues to fall down under the gravity force. In addition, the circulative motion appears behind the solid obstacles. Finally, at around t = 70 the fingers are beginning to form trapped bubbles and self-intersection of the interface occurs.

In order to assess the influince of the viscosity on the interface dynamics, two additional numerical tests were performed, with  $\mu^-=1$ ,  $\mu^+=2$ , and  $\mu^-=2$ ,  $\mu^+=1$ , correspondigly. The rest of the parameters and domain configuration were kept the same as in Test problem 1.

As expected, the higher viscosity in the upper fluid has a stabilizing effect on the dynamics of the interface, Figure 12. At the same time, the increase in the viscosity of the

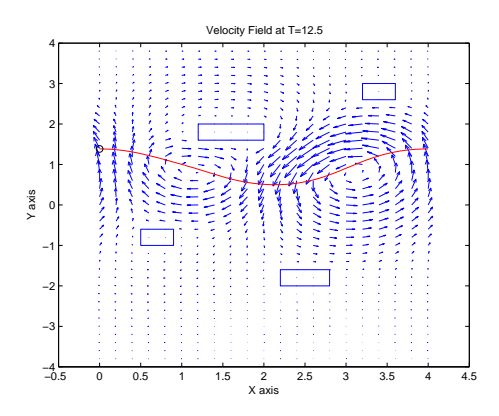


Figure 6: The velocity field and interface  $\Gamma$  for test case 1 using  $80 \times 160$  uniform mesh at t=12.5.

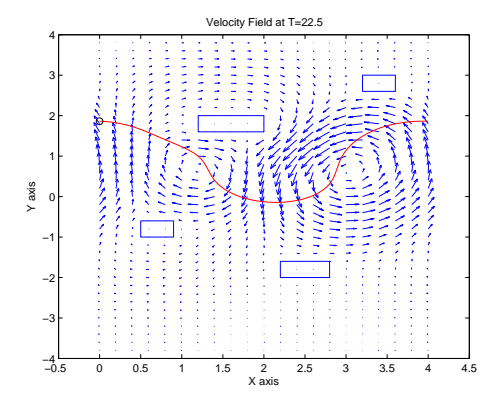


Figure 7: The velocity field and interface  $\Gamma$  for test case 1 using  $80 \times 160$  uniform mesh at t=22.5.

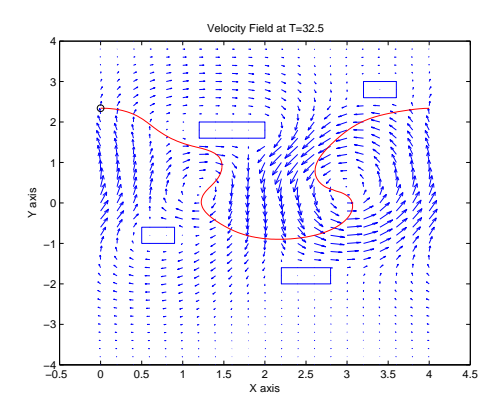


Figure 8: The velocity field and interface  $\Gamma$  for test case 1 using  $80 \times 160$  uniform mesh at t=32.5.

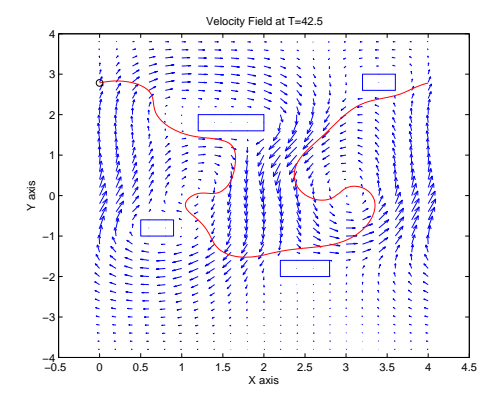


Figure 9: The velocity field and interface  $\Gamma$  for test case 1 using  $80 \times 160$  uniform mesh at t=42.5.

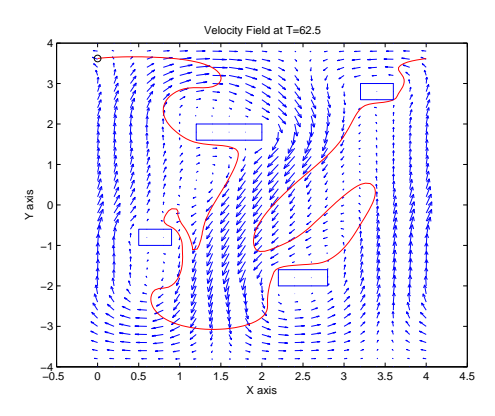


Figure 10: The velocity field and interface  $\Gamma$  for test case 1 using  $80 \times 160$  uniform mesh at t=62.5.

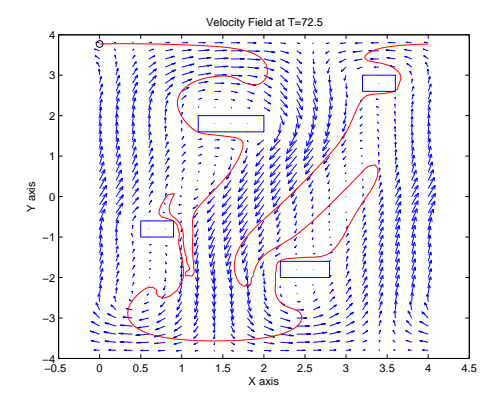


Figure 11: The velocity field and interface  $\Gamma$  for test case 1 using  $80 \times 160$  uniform mesh at t = 72.5.

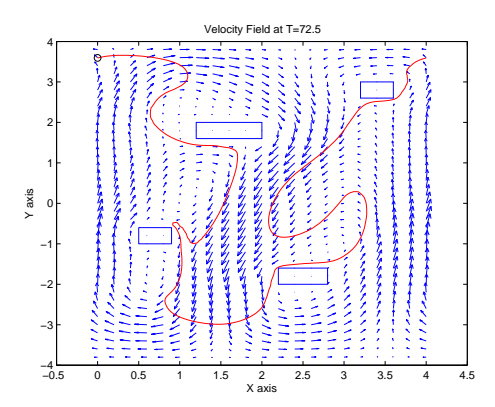


Figure 12: The velocity field and interface  $\Gamma$  for test case 1 with  $\mu^-=2, \ \mu^+=1$  using  $80\times 160$  uniform mesh at t=72.5.

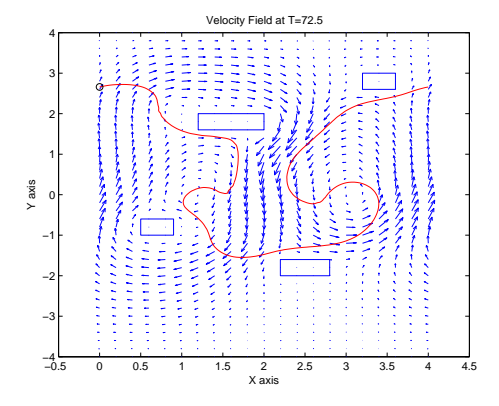


Figure 13: The velocity field and interface  $\Gamma$  for test case with  $\mu^-=1, \ \mu^+=2$  using  $80\times 160$  uniform mesh at t=72.5.

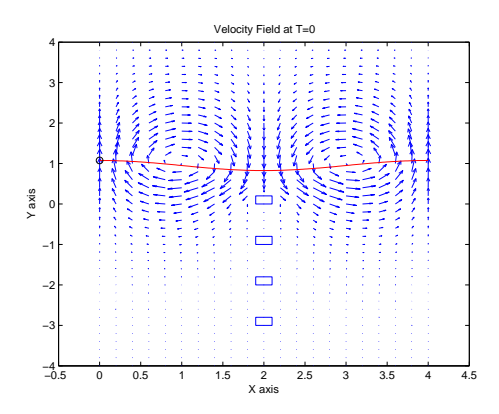


Figure 14: The velocity field and interface  $\Gamma$  for test case 2 using  $80 \times 160$  uniform mesh at t = 0.

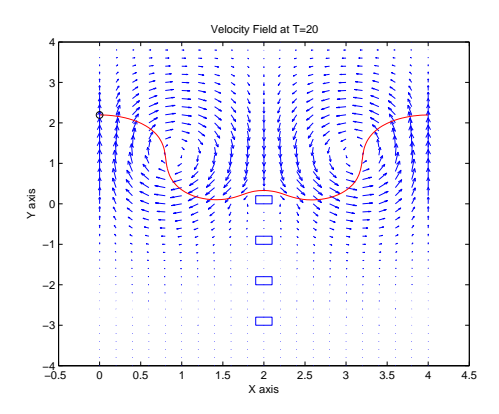


Figure 15: The velocity field and interface  $\Gamma$  for test case 2 using  $80 \times 160$  uniform mesh at t = 20.

lower fluid seems to decrease the propagation speed of the interface and velocity field in general.

#### 4.2 Test problem 2

In the second test problem we consider a configuration where the solid obstacles of the same size are situated symmetric along the axis of symmetry x=2. The initial position of the interface, computational domain, boundary conditions and the physical parameters of the problem are the same as in test case 1. Similar to the test case 1 the density gradient spawns the formation of two vortexes, the heavy fluid is sinking and the light fluid is rising, see Figures 14-16.

As we can see from the numerical results, the symmetry in the flow is preserved only for a short while. Already at t = 60 the symmetry starts to detoriarate and is totally lost by

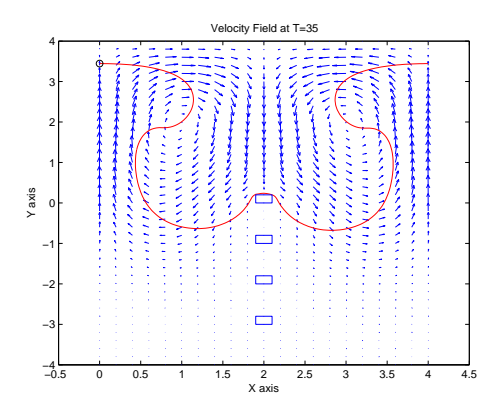


Figure 16: The velocity field and interface  $\Gamma$  for test case 2 using  $80 \times 160$  uniform mesh at t=35.

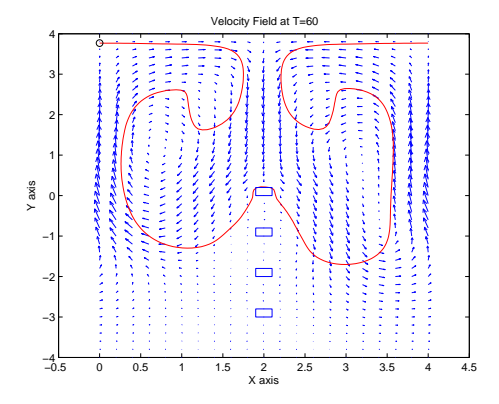


Figure 17: The velocity field and interface  $\Gamma$  for test case 2 using  $80 \times 160$  uniform mesh at t=60.

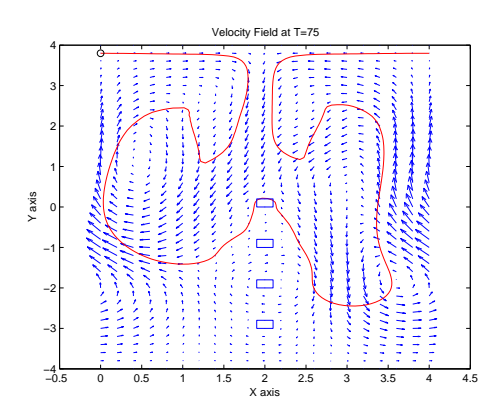


Figure 18: The velocity field and interface  $\Gamma$  for test case 2 using  $80 \times 160$  uniform mesh at t = 75.

t=75. As a consequence additional, artificial vortexes are formed and the solution loses its validity. Most probably, this behavior of the solution is induced by the unsymmetry in the mesh that is amplified by the unstable nature of the problem at hand. These artificial solutions are usually referred in the literature as "ghost solutions" since they never appear as solutions of partial differential equations but only in discrete approximations. Similar results on unsymmetric meshes applied to RT instability problem have been reported in [26].

In order to preserve the symmetry invariant in the solution, we introduce an additional procedure, that can be seen as a projection of the solution to the subspace consisting of the symmetric solutions to our interface problem. The procedure itself consists of flipping the interface from left to right, and taking a mean between the original velocity and the one obtained with the flipped interface as a resulting velocity field. An alternative to this approach would be to consider a symmetric discretization, such as , for example, a union-jack mesh, see [26].

As we can see from Figures 19-24 the modified solution retains the symmetry at all moments in time. Qualitively, we should point out the formation of the trailing vortexes behind the solid obstacles that induces circulative motions of the fluid, see Figures 22-24. Also, note the necking effect of the heavy fluid in the upper part of the domain, that eventually lead to self-intersection of the interface at t=140. Additional topology changes are also emerging in other parts of the computational domain.

## 5 Conclusions

In this paper, an extension of the immersed finite element method for the interface Stokes problems was presented. It has been shown that triangulation of the computational domain  $\Omega$  that is used in the introduced immersed finite element method can be formed without consideration of the interface location. In addition, the immersed finite element spaces are

5 CONCLUSIONS

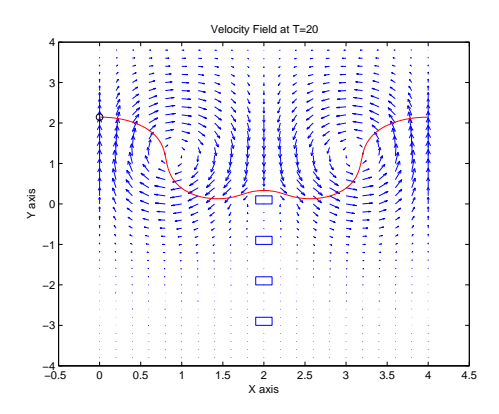


Figure 19: The modified velocity field and interface  $\Gamma$  for test case 2 using  $80 \times 160$  uniform mesh at t = 20.

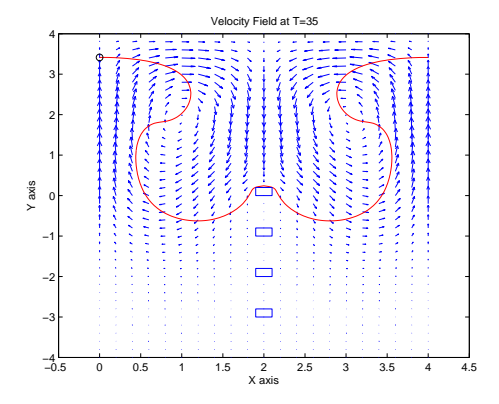


Figure 20: The modified velocity field and interface  $\Gamma$  for test case 2 using  $80 \times 160$  uniform mesh at t=35.

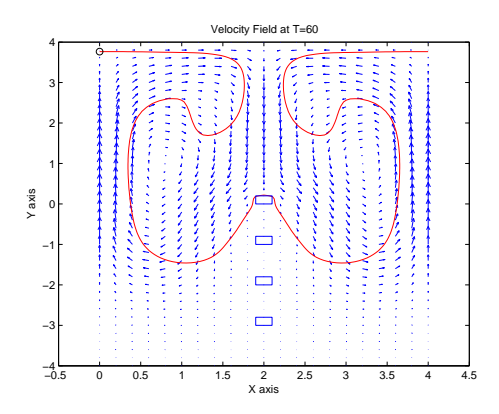


Figure 21: The modified velocity field and interface  $\Gamma$  for test case 2 using  $80 \times 160$  uniform mesh at t = 60.

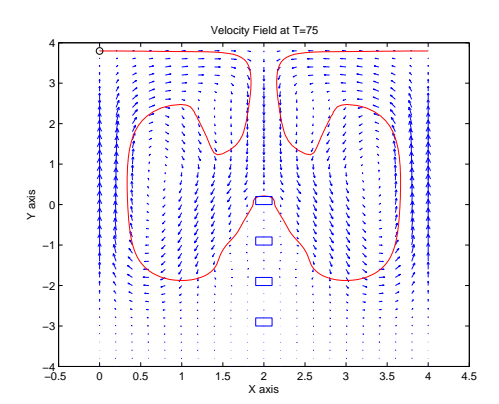


Figure 22: The modified velocity field and interface  $\Gamma$  for test case 2 using  $80 \times 160$  uniform mesh at t = 75.

5 CONCLUSIONS

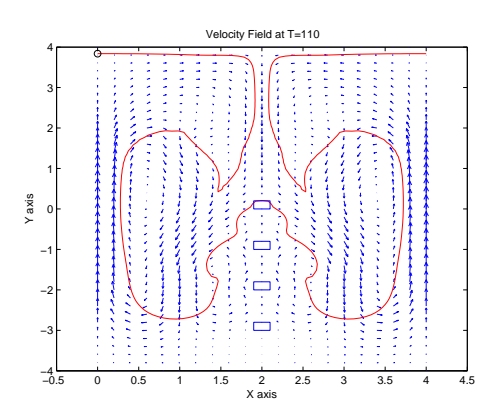


Figure 23: The modified velocity field and interface  $\Gamma$  for test case 2 using  $80 \times 160$  uniform mesh at t = 110.

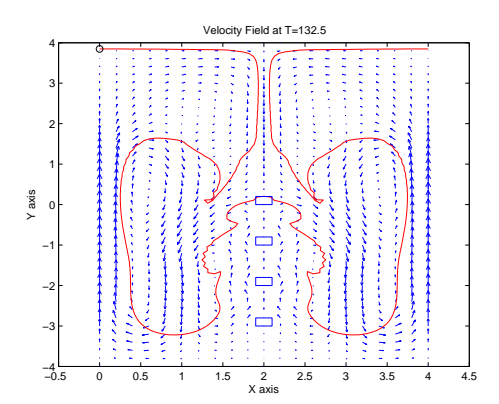


Figure 24: The modified velocity field and interface  $\Gamma$  for test case 2 using  $80 \times 160$  uniform mesh at t = 132.

closely related to the standard finite element spaces used for solution of the Stokes problem except for the elements of the partition that are intersected by the interface. Over the set of the intersected elements, the immersed finite element function are modified according to the jump conditions on the interface, that were derived from the problem itself. The interface representation and its interaction with the flow has been described in detail.

The proposed method was later applied to the solution of the Rayleigh-Taylor instability flow problem with solid obstacles. It has been shown that the introduced method can handle well both the discontinuity of the physical fields and singular forces. The method proved to be second order accuracy and mass conservative. Based on the numerical experiments, the qualitive description of the interface dynamics for the considered test cases has been given. The numerical results suggested that the discretization errors are systematically amplified by the instability of the problem at hand, and thus affect, in the long run, both the convergence results and the symmetry of the solution. The symmetry preserving version of the method has also been proposed and successfully tested.

Future work points in several directions from the current stand. One is the theoretical investigation of the introduced non-conforming finite element method. The other is the improvement of the method itself, with the primary focus on developing the ability to capture the topological changes in the interface. Finally, it would be intriguing to apply the developed method to some more realistic applications.

28 REFERENCES

## References

[1] J.F. Barnes, D.H. Janney, R.K. London, K.A. Meyer, and D.H. Sharp. Further experimentation on taylor instability in solids. *J. Appl. Phys.*, 51:4678–4679, 1980.

- [2] D. Braess. Finite elements. theory, fast solvers, and applications in solid mechanics. Cambridge university press, 1997.
- [3] Z. Chen and J. Zou. Finite element methods and their convergence for elliptic and parabolic interface problems. *Numer. Math.*, 79:175–202, 1998.
- [4] V.G. Danilov and G.A. Omelyanov. Estimate for the width of the mushy region between two liquids of different densities. *Preprint, Universidade da Beira Interior, Portugal*, 1999.
- [5] V.G. Danilov and G.A. Omelyanov. Dynamics of the interface between two immiscible liquids with nearly equal densities under gravity. *Euro. Jnl. of Applied Math.*, 13:497–516, 2002.
- [6] R.E. Duff, F.H. Harlow, and C.W. Hirt. Effects of diffusion on interface instability between gases. *Phys. Fluids*, 5:417–425, 1962.
- [7] H.W. Emmons, C.T. Chang, and B.C. Watson. Taylor instability of finite surface waves. J. Fluid Mech., 7:177–193, 1960.
- [8] Y. Fraigneau, J. Guermond, and L. Quartapelle. Approximation of variable density incompressible flows by means of finite elements and finite volumes. *Communications in Numerical methods in Engineering*, 17:893–902, 2001.
- [9] S.Y. Gertsenstein and B.M. Cherniavskii. Nonlinear evolution of two- and three-dimensional perturbations under the rayleigh-taylor instability. *Izv. Akad. Nauk. USSR*, *Mekh. Zhidk. Gaza*, 2:38–46, 1985.
- [10] J. Glimm, X.L. Li, R. Menikoff, D.H. Sharp, and Q. Zhang. A numerical study of bubble interactions in rayleigh-taylor instability for compressible fluids. *Phys. Fluids* A, 2:2046–2054, 1990.
- [11] C.W. Hirt and B.D. Nichols. Volume of fluid (vof) method for the dynamics of free boundaries. *J. Comput*, 39:201–225, 1981.
- [12] D.J. Lewis. The instability of liquid surfaces when accelerated in a direction perpendicular to their planes. *Proc. R. Soc. London Ser.*, A 202:81–96, 1950.
- [13] Z. Li. The immersed interface method using a finite element formulation. *Appl. Num. Math.*, 27:253–267, 1998.
- [14] Z. Li, T. Lin, and X. Wu. New cartesian grid methods for interface problems using finite element formulation. NSCU CRSC-TR99-5, 1999.

REFERENCES 29

[15] A. Loubenets. A new finite element method for elliptic interface problems. *Licenciate thesis*, Royal Institute of Technology, NADA, 2006.

- [16] A. Loubenets, T. Ali, and M. Hanke. Highly accurate finite element method for one-dimensional elliptic interface problems. *submitted in Applied Numerical Mathematics*, 2006.
- [17] A. Loubenets and M. Hanke. An immersed finite element method and its convergence for elliptic interface problems with discontinuous coefficients and singular sources. TRITA, 2007.
- [18] R. Popil and F.L. Curzon. Production of reproducible rayleigh-taylor instabilities. Rev. Sci. Instr., 50:1291–1295, 1979.
- [19] S. Popinet and S. Zaleski. A front-tracking algorithm for accurate representation of surface forces. *International Journal of Numerical Methods in Fluids*, 30:775–793, 1999.
- [20] G.E. Puckett, A.S. Almgren, J.B. Bell, D.L. Marcus, and J. Rider. A high-order projection method for tracking fluid interfaces in variable density incompressible flows. *Journal of Computational Physics*, 130:269–282, 1982.
- [21] W.J. Rider and D.B. Kothe. Reconstructing volume tracking. *Journal of Computational Physics*, 141:112, 1998.
- [22] M. Rudman. Volume-tracking methods for interfacial flow calculations. *Int.J.Numer.methods Fluids*, 24:671, 1997.
- [23] R. Scardovelli and S. Zaleski. Direct numerical simulation of free-surface and interfacial flow. Annu. Rev. Fluid Mech, 31:567–603, 1999.
- [24] D.H. Sharp. An overview of rayleigh-taylor instability. *Physica D.*, 12:3–18, 1984.
- [25] A. Smolianski. Finite-element/level-set/operator-splitting (felsos) approach for computing two-fluid unsteady flows with free moving interfaces. *International Journal for Numerical Methods in Fluids*, 48:231–269, 2005.
- [26] M. Tabata. Numerical simulation of rayleigh-taylor problems by an energy-stable finite element scheme. MHF 2006-1, Kyushu University Fukuoka, Japan, 2006.
- [27] G. Tryggvason, B. Bunner, A. Esmaeeli, D. Juric, W. Tauber N. Al-Rawahi, J. Han, S. Nas, and Y.-J. Jan. A front-tracking method for the computations of multiphase flow. *J. Comput. Phys.*, 169:708–759, 2001.
- [28] G. Tryggvason and S.O. Unverdi. Computations of three dimensional rayleigh-taylor instability. *Phys. Fluids A*, 2:656–659, 1990.

[29] S.O. Unverdi and G. Tryggvason. A front tracking method for viscous, incompressible, multi-fluid flows. *J. Comput. Phys.*, 100:25–37, 1992.

- [30] D.L. Young. Time dependent multi-material flow with large fluid distortion. *Numerical Methods for Fluid Dynamcis*, pages 273–285, 1982.
- [31] Y. Zhao, H.H. Tan, and B. Zhang. A high-resolution characteristics-based implicit dual time-stepping vof method for free surface flow simulation on unstructured grids. *Communications in Numerical Methods and Engineering*, 183:233–273, 2001.
- [32] J. Zhu and J.A. Sethian. Projection methods coupled to level set interface techniques. Journal of Computational Physics, 102:128, 1992.